Article:

Yuksel, C. and Lesnic, D. orcid.org/0000-0003-3025-2770 (2024) The identification of obstacles immersed in a steady incompressible viscous fluid. Journal of Engineering Mathematics, 144 (1). 16. ISSN 0022-0833

https://doi.org/10.1007/s10665-023-10323-1

The identification of obstacles immersed in a steady incompressible viscous fluid

G. Yuksel[1,2] and D. Lesnic[2]
[1]*Department of Mathematics, Faculty of Science, Mugla Sitki Kocman University, Mugla, Turkey*
[2]*Department of Applied Mathematics, University of Leeds, Leeds, LS2 9JT, UK*

Abstract.
In this paper, the identification of immersed obstacles in a steady incompressible Navier-Stokes viscous fluid flow from fluid traction measurements is investigated. The solution of the direct problem is computed using the finite element method (FEM) implemented in the Freefem++ commercial software package. The solution of the inverse geometric obstacle problem (parameterized by a small set of unknown constants) is accomplished iteratively by minimizing the nonlinear least-squares functional using an adaptive moment estimation algorithm. The numerical results for the identification of an obstacle in a viscous fluid flowing in a channel with open ends, show that when the fluid traction is measured on the top, bottom and inlet boundaries, then the algorithm provides accurate and robust reconstructions of an obstacle parameterized by a small number of parameters in a Fourier trigonometric finite expansion. Stable reconstructions with respect to noise in the measured fluid traction data are also achieved, although for complicated shapes parameterized by larger degrees of freedom nonlinear Tikhonov regularization of the least-squares functional may need to be employed. Multiple-component obstacles may also be identified provided that a good initial guess is provided. In case of limited data being available only at the inlet boundary the pressure gradient provides more information for inversion than the fluid traction.

Keywords: Inverse geometry problems; Navier-Stokes equations; Finite element method; Fluid flows.

1 Introduction

The identification of obstacles immersed in fluids has significant implications in various domains, including environmental monitoring, medical imaging, submersed vehicles or aquatic mine detection. And just as a timely application, the very recent dam destruction in Ukraine resulted in initially buried landmines becoming underwater floating and needed to be detected. Nevertheless, direct observation or measurement of submerged objects is often challenging or impossible. In such a situation, inverse modeling offers a valuable approach to overcome these challenges by utilizing observed effects or indirect measurements to infer the properties, shapes, sizes and locations of submerged obstacles. There are several papers about the identification of obstacles immersed in some different types of fluids such as, potential [5], Stokes [18, 3, 2], Oseen [15, 11], Brinkman [12, 13] or Navier-Stokes [1, 7]. The studies in [1, 7] were mainly theoretical and they dealt with the simpler Dirichlet boundary conditions for which the existence and uniqueness of solution theory is available [23]. However, in our study, we consider a more physical scenario in which the unknown obstacle is placed in an open end channel containing a viscous fluid. For this situation, mixed boundary conditions are appropriate, and this distinguishes from the previous studies [1, 7] in which only Dirichlet boundary conditions were investigated. As for the extra measurement required to compensate for the missing information on the concealed obstacle we consider the partial knowledge of the fluid traction on a sub-portion of the boundary where Dirichlet conditions are prescribed (no-slip or inlet fluid velocity). For one example, we also investigate the possibility of measuring the pressure gradient at the inlet boundary, as proposed in [7].

The plan of the paper is as follows. First, the mathematical formulation and FEM numerical results for the direct problem are presented in Section 2. Next, in Section 3, the inverse geometric obstacle problem is introduced and the numerical method based on minimizing the gap between the computed and measured data using the adaptive moment estimation algorithm of [14] is described. In Section 4, several numerical results on obstacle identification are presented and discussed with respect to the initial guess, noise in the measured data, limited data and multiple component obstacles. Furthermore, boundary pressure gradient measurements at the inlet are also inverted. Finally, Section 5 highlights the conclusions of the paper.

2 Mathematical formulation of the direct problem

Consider a bounded and connected domain $\Omega \subset \mathbb{R}^d$, $(d = 2, 3)$, containing an unknown fixed object/obstacle D (such that $\Omega\backslash\overline{D} =: \Omega_0$ is connected) in between which a steady incompressible viscous fluid flows. We assume that the boundary $\partial(\Omega\backslash D) = \partial\Omega \cup \partial D$ is sufficiently smooth. If the obstacle D is known, then the direct problem associated with this fluid flow situation, in non-dimensionless variables, is given by [6]:

$$-\nu\triangle\boldsymbol{u} + (\boldsymbol{u}\cdot\nabla)\boldsymbol{u} + \nabla p = \boldsymbol{0} \quad \text{in } \Omega_0, \tag{1}$$

$$\nabla\cdot\boldsymbol{u} = 0 \quad \text{in } \Omega_0, \tag{2}$$

$$\boldsymbol{u} = \boldsymbol{u}_{in} \quad \text{on } \Gamma_{in}, \tag{3}$$

$$\boldsymbol{u} = \boldsymbol{0} \quad \text{on } \Gamma_{top}\cup\Gamma_{bottom}\cup\partial D, \tag{4}$$

$$\boldsymbol{t} = \boldsymbol{0} \quad \text{on } \Gamma_{out}, \tag{5}$$

where $\boldsymbol{u}$ is the fluid velocity, p is the fluid pressure, ν is the kinematic viscosity of the Newtonian viscous fluid,

$$\boldsymbol{t} = \sigma(\boldsymbol{u}, p)\boldsymbol{n} \tag{6}$$

is the fluid traction, $\boldsymbol{n}$ is the outward unit normal to the boundary $\partial\Omega_0$,

$$\sigma(\boldsymbol{u}, p) = 2\nu e(\boldsymbol{u}) - p\boldsymbol{I} \tag{7}$$

is the stress tensor, $\boldsymbol{I}$ is the identity,

$$e(\boldsymbol{u}) = \frac{1}{2}(\nabla\boldsymbol{u} + (\nabla\boldsymbol{u})^{\mathrm{T}}) \tag{8}$$

is the strain tensor, $\boldsymbol{u}_{in}$ is the fluid velocity at the inlet boundary Γ_{in} and the boundary $\partial\Omega_0 = \Gamma_{in}\cup\Gamma_{top}\cup\Gamma_{bottom}\cup\Gamma_{out}\cup\partial D$, see Figure 1. In equation (5), the so-called, 'do-nothing' artificial boundary condition expresses that the outlet boundary Γ_{out} is traction-free. In equation (1), the coefficient ν is proportional with the inverse of the Reynolds number Re, which indicates the regime type of flow, e.g., laminar at low Re (i.e., high ν) where viscous effects are prevailing; or turbulent at high Re (i.e., low ν) where convective effects are dominant [19].

Based on (2), (7) and (8), equation (1) can be re-written in the equivalent form:

$$-\nabla\cdot\sigma(\boldsymbol{u}, p) + (\boldsymbol{u}\cdot\nabla)\boldsymbol{u} = \boldsymbol{0} \quad \text{in } \Omega_0, \tag{9}$$

which is more suitable for formulating the weak form of the problem (1)-(5). The weak form of the direct problem (1)-(5) is formulated as follows. Given $\boldsymbol{u}_{in} \in H^{1/2}(\Gamma_{in})$, the pair $(\boldsymbol{u}, p) \in (H^1(\Omega_0))^d \times L^2(\Omega_0)$ is called a weak solution for the direct problem (1)-(5) if $\boldsymbol{u}$ satisfies the Dirichlet boundary conditions (3) and (4) and

$$\left.\begin{array}{l} a(\boldsymbol{u},\boldsymbol{v}) + b(\boldsymbol{v},p) = 0 \\ b(\boldsymbol{u},q) = 0 \end{array}\right\} \quad \forall(\boldsymbol{v},q) \in (H^1(\Omega_0))^d \times L^2(\Omega_0) \text{ with } \boldsymbol{v}|_{\partial\Omega_0\setminus\Gamma_{out}} = \mathbf{0}, \tag{10}$$

where

$$a(\boldsymbol{u},\boldsymbol{v}) = 2\nu \int_\Omega e(\boldsymbol{u}) : e(\boldsymbol{v})\mathrm{d}x + \int_\Omega (\mathbf{u}\cdot\nabla)\boldsymbol{u}\cdot\boldsymbol{v}\mathrm{d}x,$$

$$b(\boldsymbol{v},p) = -\int_\Omega p\nabla\cdot\boldsymbol{v}\mathrm{d}x, \quad b(\boldsymbol{u},q) = -\int_\Omega q\nabla\cdot\boldsymbol{u}\mathrm{d}x$$

and : denotes the Frobenius inner product of two matrices $e(\boldsymbol{u}) : e(\boldsymbol{v}) = \sum_{i,j=1}^d e_{ij}(\boldsymbol{u})e_{ij}(\boldsymbol{v})$, [16]. Results on the existence and uniqueness of the solution to the direct mixed problem (1)-(5), understood in the weak sense (10), are unknown at present, but they are expected to hold if the viscosity ν is large enough, i.e., for sufficiently low Re number, by combining the arguments in [7, 6, 23, 4, 8, 10].

Based on the weak formulation (10), the solution of the direct problem (1)-(5) is computed numerically using the finite element method (FEM) implemented in the Freefem++ package [9].

2.1 Numerical results and discussion for the direct problem

For numerical illustration and discussion, let us consider $\Omega = (-L, L) \times (-H, H)$ with $L = 7.5$ and $H = 2.5$ (modelling a channel of width $2H$ with open ends) and a circle-shaped obstacle D of radius $r = 0.5$ centred at $(x_0, y_0) = (-3, 0)$ in this domain. The kinematic viscosity is taken $\nu = \frac{1}{10}$ so, $Re = \frac{1}{\nu} = 10$. This situation models the laminar viscous flow past a circular cylinder in the domain Ω. The input fluid velocity at the inlet Γ_{in} in (3) is taken as the Poiseuille-type parabolic profile $\boldsymbol{u}_{in} = \big(1 - (\frac{y}{H})^2, 0\big)$ for $y \in (-H, H)$.

First, in order to show that the independence of the FEM mesh size was achieved, the components of the traction vector $\boldsymbol{t} = (t_1, t_2)$ on the sub-boundary $\Gamma := \Gamma_{bottom} \cup \Gamma_{top} \cup \Gamma_{in}$ are compared for $m \in \{5, 10, 20\}$ in Figure 2, where the boundaries Γ_{top}, Γ_{bottom} and ∂D are uniformly discretised into $3m$ elements each, whilst the boundaries Γ_{top} and Γ_{bottom} are uniformly discretised into $2m$ elements each. This boundary discretisation with $13m$ elements generates a FreeFem++ domain discretisation with $\{421, 1622, 6648\}$ triangles and $\{243, 876, 3454\}$ vertices for $m \in \{5, 10, 20\}$, respectively. From Figure 2 it can be seen that all curves overlap showing that the independence of the mesh has been achieved.

Next for the mesh size $m = 20$, the numerically obtained pressure and velocity fields in the fluid domain are illustrated in Figures 3b and 3c, respectively, along with the finite element mesh shown in Figure 3a. These viscous flow fields are typical to a laminar fluid regime at a relatively low Reynolds number [22].

3 Inverse geometric problem

In the inverse problem, the obstacle D concealed in the channel Ω is unknown and has to be detected from measurements of the fluid traction on a subset Γ_0 of the boundary $\partial\Omega_0 \backslash \Gamma_{out}$, namely,

$$\boldsymbol{t} = \boldsymbol{t}^{exp} \quad \text{on } \Gamma_0. \tag{11}$$

Alternatively, one could measure the fluid velocity $\boldsymbol{u}_{out}$ at the outlet boundary Γ_{out}, [6]. The measurement (11) was also considered in [2] for the simpler linear case of slow viscous Stokes fluid flow. The uniqueness of solution $(\boldsymbol{u}, p, D)$ of the inverse problem (1)-(5) and (11) under the assumptions that Ω_0 is connected, $\boldsymbol{u}_{in} \not\equiv \mathbf{0}$ and ν is sufficiently large could follow along the lines of the proof of Theorem 1.2 of [7] for the Dirichlet problem (in which the Neumann boundary condition (5) is replaced by the homogeneous Dirichlet boundary condition $\boldsymbol{u} = \mathbf{0}$ on Γ_{out}).

In the remaining of the paper, we consider the two-dimensional case $d = 2$. Also assume that the unknown obstacle D is star-shaped with respect to an unknown center $\mathbf{c}_0 := (x_0, y_0)$, whose boundary is parametrized by

$$\partial D = \{\mathbf{c}_0 + r(\theta)(\cos(\theta), \sin(\theta)) | \theta \in [0, 2\pi)\}, \quad \text{where } r(\theta) = a_0 + \sum_{k=1}^{J} \{a_k \cos(\theta) + b_k \sin(\theta)\}. \tag{12}$$

For solving the inverse problem (1)-(5) and (11) to detect the obstacle (12), we minimize the least-squares functional

$$f(\boldsymbol{\Theta}) := ||\boldsymbol{t}(\boldsymbol{\Theta}) - \boldsymbol{t}^{exp}||^2, \tag{13}$$

where $(\Theta_k)_{k=\overline{1,(2J+3)}} = \boldsymbol{\Theta} = (x_0, y_0, (a_i)_{i=\overline{0,J}}, (b_i)_{i=\overline{1,J}})$ is a vector containing the $(2J+3)$ unknowns and $\boldsymbol{t}(\boldsymbol{\Theta})$ is the numerical solution for the fluid traction on Γ_0 of the direct problem (1)-(5) for a given $\boldsymbol{\Theta}$. The minimization of (13), subjected to the constraint that the obstacle D stays within the domain Ω throughout the iteration process, was initially attempted using a classical gradient descent method but the results were found strongly dependent on the initial guess and time-consuming. In order to achieve higher performance, the adaptive moment estimation algorithm of [14], summarised below, was employed, at the price of increasing the number of hyperparameters to be selected.

Iterative algorithm [14]:

- Input the hyperparameters β_1, $\beta_2 \in [0, 1)$, $\epsilon > 0$ and the learning rate $\boldsymbol{\alpha}$. The hyperparameters β_1 and β_2 represent the exponential decay rates for the first and second-moment estimates, respectively, whilst the (machine) learning rate $\boldsymbol{\alpha}$ is nothing else than the usual stepsize in a gradient descent method.
- Start the iterative process with an initial guess $\boldsymbol{\Theta}_n = ((\Theta_k)_n)_{k=\overline{1,(2J+3)}}$ at iteration $n = 0$.
- Initialize the first moment vector $\mathbf{m}_0 = \mathbf{0}$ and the second moment vector $\mathbf{v}_0 = \mathbf{0}$.

```
• While $f(\boldsymbol{\Theta}_n) > \delta$ do
$n \leftarrow n + 1$
$\mathbf{g}_n = \nabla f(\boldsymbol{\Theta}_n)$
$\mathbf{m}_n = \beta_1 \mathbf{m}_{n-1} + (1 - \beta_1)\mathbf{g}_n,\ \hat{\mathbf{m}}_n = \mathbf{m}_n / (1 - \beta_1^n)$
$\mathbf{v}_n = \beta_2 \mathbf{m}_{n-1} + (1 - \beta_2)\mathbf{g}_n^2,\ \hat{\mathbf{v}}_n = \mathbf{v}_n / (1 - \beta_2^n)$
```

```
$\boldsymbol{\Theta}_n = \boldsymbol{\Theta}_{n-1} - \boldsymbol{\alpha}\hat{\mathbf{m}}_n/(\sqrt{\hat{\mathbf{v}}_n} + \epsilon)$
enddo;
```

The iterations are stopped once

$$f(\boldsymbol{\Theta}_{\mathbf{n_f}}) \leq \delta \ := ||\boldsymbol{t}^{exact} - \boldsymbol{t}^{exp}||^2, \tag{14}$$

where n_f denotes the final iteration number.

In the above, all the operations involving vectors are understood element-wise, e.g., $\mathbf{g}_n^2 = \left(\left[\frac{\partial f}{\partial \Theta_k}(\boldsymbol{\Theta}_n)\right]^2\right)_{k=\overline{1,(2J+3)}}$ and $\sqrt{\hat{\mathbf{v}}_n} = \left(\sqrt{(\hat{v}_k)_n}\right)_{k=\overline{1,(2J+3)}}$. The objective functional (14) is stochastic in case the experimental data (11) is contaminated by random noise (see section 3.2 below). The gradient of the objective function (13) is calculated using forward finite difference with step size $h > 0$. Although never published in an internationally refereed journal, the above optimization algorithm (also known as adaptive first- and -second-order moment estimation ('adam')) has shown some success in terms of fast convergence and escape from local minima, and it can be used as an alternative or combined with the stochastic gradient descent method. Other algorithms reviewed in [21] may also be employed.

3.1 Parameter selection

We usually take the number of terms J in the expansion (12) small, e.g., $J = 0$ or 1, such that the number of unknowns in the vector $\boldsymbol{\Theta}$ is 3 or 5, respectively. Since the number of unknowns is small, common practice [20] suggests that this model reduction assists in aleviating the instability of the inverse problem with respect to errors in the measured data (11), and therefore no regularization is usually needed to penalize the least-squares functional (13). The mesh size is $m = 20$ for the solution of the direct problem that is employed first to numerically simulate the fluid traction data (11) necessary for solving the inverse problem. In order to avoid committing an inverse crime, for solving the inverse problem we employ a different mesh size with $m = 10$ as an iterative direct FEM solver. The maximum number of iterations is taken as 5000. The hyper-parameters are taken as $\beta_1 = 0.9$, $\beta_2 = 0.99$ and $\epsilon = 10^{-8}$, as suggested by [14]. The learning rate $\boldsymbol{\alpha}$ and the finite-difference step size h employed in calculating the gradient of the objective function are selected by trial and error.

3.2 Noisy data

In order to simulate that the practical measurement (11) of the fluid traction on Γ_0 is inherently inexact, we add noise to the traction values on Γ_0 as $\boldsymbol{t}^{exp} = (1+\zeta\rho)\boldsymbol{t}$, where ζ are pseudo-random numbers generated from a uniform distribution in $[-1, 1]$ and ρ represents the percentage of noise with which the data (11) is contaminated. Note that the threshold δ in (14) will depend on ρ.

4 Numerical results and discussion for the inverse problems

Corresponding to the geometry and input data of the example discussed in subsection 2.1, in this section, we present several examples to identify unknown star-shaped obstacles D concealed in the domain Ω. In the Examples 4.1-4.3, traction vector values are measured on $\Gamma_0 = \Gamma$, whilst in Example 4.4, we consider limited traction vector data measured on $\Gamma_0 = \Gamma_{in}$ only. In Example 4.4, we also consider the case when the fluid traction data (11) on $\Gamma_0 = \Gamma_{in}$ is replaced by the pressure gradient measurement [7],

$$\nabla p = \boldsymbol{q}^{exp} \quad \text{on } \Gamma_{in}. \tag{15}$$

Example 4.1. First, we consider an example to identify a simple target D consisting of a circle of radius $a_0 = 0.5$ centered at $(x_0, y_0) = (-3, 0)$. The fluid traction (11), numerically simulated and illustrated in Figure 2, as described in subsection 3.1, is considered measured over the sub-boundary $\Gamma_0 = \Gamma = \Gamma_{top} \cup \Gamma_{bottom} \cup \Gamma_{in}$. We consider two different initial guesses; one of them is at the center $(0, 0)$ and the other one is at the top-right-hand side $(5, 1)$ of the domain Ω. The forward finite difference step size h for calculating the gradient of (13) is taken as 0.01, which was found sufficiently small to ensure that any further decrease in this parameter did not significantly affect the accuracy of the numerical results. Also, the learning rate vector $\boldsymbol{\alpha} = (lrx_0, lry_0, lra_0)$ is prescribed (by trial and error) as $(0.01, 0.001, 0.001)$. The values of the noise threshold are

$$\delta(\rho) \in \{0.024, 0.068, 0.130\} \quad \text{for} \quad \rho \in \{0, 5, 10\}\%, \tag{16}$$

respectively. Note that in case $\rho = 0$, although there is no random noise added to the data, because of the way the fluid traction data has been fabricated to avoid committing an inverse crime, as described in subsection 3.1, there still exists some numerical noise that is present.

(a) The initial guess for the parameter of unknowns is first $(x_0^0, y_0^0, a_0^0) = (0, 0, 0.3)$. With this initial guess, the stopping iteration numbers based on the criterion (14) with δ given by (16) are

$$n_f(\rho) \in \{324, 612, 403\} \quad \text{for} \quad \rho \in \{0, 5, 10\}\%, \tag{17}$$

respectively. In case of no noise, the convergences of the objective function (13) and of the parameters $\boldsymbol{\Theta} = (x_0, y_0, a_0)$ with the number of iterations $n = \overline{1, n_f}$ are illustrated in Figure 4. The history of the target obstacle as it moves through the iteration process is illustrated in Figure 5. The target parameters recovered after $n_f(\rho)$ final iterations given by (17) for $\rho \in \{0, 5, 10\}\%$ noise are included in Table 1. Overall, from Figures 4 and 5 and Table 1 it can be seen that accurate and stable recoveries of the circular obstacle have been achieved.

(b) Next, we consider a farther initial guess of the center of the circular obstacle located at $(x_0^0, y_0^0) = (5, 1)$ and we keep the same initial guess $a_0^0 = 0.3$ for the radius. With this initial guess, the stopping iteration numbers are obtained as

$$n_f(\rho) \in \{1162, 1349, 1112\} \quad \text{for} \quad \rho \in \{0, 5, 10\}\%, \tag{18}$$

respectively. In case of no noise, the convergences of the objective function (13) and of the parameters $\mathbf{\Theta} = (x_0, y_0, a_0)$ with the number of iterations $n = \overline{1, n_f}$ are illustrated in Figure 6. The targets and parameters recovered after $n_f(\rho)$ final iterations given by (18) for $\rho \in \{0, 5, 10\}\%$ noise are included in Figure 7 and Table 2. As in case (a), accurate and stable results can be observed.

The numerical results investigated in cases (a) and (b) for two different initial guesses (and also for many others not presented) conclude that the numerical method of section 3 is robust by being independent of the initial guess in case of searching for a circular obstacle of unknown centre and size (radius).

Example 4.2. In the second example, we consider a cardioid shape as the target obstacle given by

$$r(\theta) = 0.5 - 0.4\cos(\theta) + 0.3\sin(\theta), \quad \theta \in [0, 2\pi), \tag{19}$$

with centre $(x_0, y_0) = (-3, 0)$. We approximate the radius $r(\theta)$ in (12) with $J = 1$. The traction vector values on $\Gamma_0 = \Gamma$ are assumed measured in (11). In this example, the center of the initial guessed obstacle is chosen close to the right-bottom part of the domain Ω, namely, at $(x_0^0, y_0^0) = (5, -1)$, while the initial guess for (a_0, a_1, b_1) is taken as $(a_0^0, a_1^0, b_1^0) = (0.3, 0, 0)$. Also, the learning rates embedded in the vector $\boldsymbol{\alpha}$ and the step size h involved in calculating the gradient of the objective function $f(\mathbf{\Theta})$ are taken as 0.01 for x_0 and y_0, and 0.001 for a_0, a_1 and b_1. The values of the noise thresholds are

$$\delta(\rho) \in \{0.006, 0.081, 0.161\} \quad \text{for} \quad \rho \in \{0, 5, 10\}\%, \tag{20}$$

respectively. With the above initial guess, the stopping iteration numbers, based on the criterion (14) with δ given by (20), are

$$n_f(\rho) \in \{1180, 1052, 626\} \quad \text{for} \quad \rho \in \{0, 5, 10\}\%, \tag{21}$$

respectively. Although the center of the initial obstacle is quite far from the exact location at $(-3, 0)$ and, compared to Example 4.1, there are two additional parameters a_1 and b_1 to be optimized for the polar radius, the method converges. The targets and parameters retrieved after $n_f(\rho)$ final iterations given by (21) for $\rho \in \{0, 5, 10\}\%$ noise are illustrated and presented in Figure 8 and Table 3. Compared to Example 4.1 where only 3 parameters had to be identified, in Example 4.2 containing 5 unknown parameters, less accurate retrieval can be observed in Table 3. In addition, for the higher amount of noise $\rho = 10\%$ instabilities set in showing that the ill-posedness of the problem starts to manifest and regularization is needed to restore stability.

Example 4.3. In this example, we consider an obstacle composed of two circles for identification. The first circle is centered at $(x_0, y_0) = (-4, 1)$ of radius $a_0 = 0.5$ and the second circle is centered at $(\tilde{x}_0, \tilde{y}_0) = (3, -1)$ of radius $\tilde{a}_0 = 0.4$. Each of the circles are approximated by (12) with $J = 0$. We start the iterations from the initial guess $(x_0^0, y_0^0, a_0^0) = (-1, 0, 0.3)$ and $(\tilde{x}_0^0, \tilde{y}_0^0, \tilde{a}_0^0) = (1, 0, 0.3)$, and learning rates $\boldsymbol{\alpha}$ and step size h all equal to 0.01. We present only the results with no noise, $\rho = 0$, which yields $\rho(0) = 0.057$ and $n_f(0) = 871$. The retrieved values at $n_f(0) = 871$ final iterations are $(x_0^{871}, y_0^{871}, a_0^{871}) = (-3.9795, 0.9128, 0.4557)$ and $(\tilde{x}_0^{871}, \tilde{y}_0^{871}, \tilde{a}_0^{871}) = (2.8319, -0.9141, 0.3576)$, which are in reasonable agreement with the exact solution $(x_0, y_0, a_0) = (-4, 1, 0.5)$ and $(\tilde{x}_0, \tilde{y}_0, \tilde{a}_0) = (3, -1, 0.4)$, respectively. The history of the double-component identified obstacle as it moves through the iteration process is illustrated in Figure 9. Reasonably accurate retrievals of the two original circles can be observed, although it is worth mentioning that the dependence on a good initial guess is more stringent for the complex two-circle multiple obstacle identification for this example than for the single obstacles investigated in the previous Examples 4.1 and 4.2.

Example 4.4. In the last example, we investigate inverting limited traction data on the inlet only, i.e. $\Gamma_0 = \Gamma_{in}$ in (11), for the geometrical configuration and data of Example 4.1. The initial guess is $a_0^0 = 0.3$ for the radius of the circle, whilst for the center we investigate three initial guesses given by: $(x_0^0, y_0^0) = (0, 0)$, $(x_0^0, y_0^0) = (-2, 0)$ and $(x_0^0, y_0^0) = (-2.5, 0)$. In this limited data case, the exact target could not be identified within the 5000 maximum number of iterations allowed. A possible reason for this may be that the values of fluid traction on Γ_{in} are very close to zero (see the last five points in Figure 2 and Table 4). A possible alternative in this case may be to measure the pressure gradient ∇p on Γ_{in}, namely,

$$\nabla p = \boldsymbol{q}^{exp} \quad \text{on} \quad \Gamma_0 = \Gamma_{in} \tag{22}$$

instead of fluid traction, which has also larger component values than traction, see Table 4. In case of Dirichlet boundary conditions

$$\boldsymbol{u} = \boldsymbol{\zeta} \ \text{ on } \partial\Omega, \quad \boldsymbol{u} = \boldsymbol{0} \ \text{ on } \partial D, \tag{23}$$

under certain assumptions, the uniqueness of the inverse problem given by equations (1), (2), (22) and (23) holds [7, Section 4].

In case of (22), instead of (13), we minimize

$$f(\boldsymbol{\Theta}) := ||\nabla p(\boldsymbol{\Theta}) - \boldsymbol{q}^{exp}||^2. \tag{24}$$

With the learning rates $\boldsymbol{\alpha} = (0.01, 0.001, 0.01)$ and $h = 0.01$ for (x_0, y_0, a_0), $\delta(0) = 0.0002$ the method converged, see Figure 10, from the initial guess $(x_0^0, y_0^0) = (-2.5, 0)$ in $n_f(0) = 293$ final iterations to $(-2.9027, -0.012, 0.5067)$, which is close to the exact target of $(-3, 0, 0.5)$. For the other two initial guesses $(x_0^0, y_0^0) = (0, 0)$ and $(x_0^0, y_0^0) = (-2, 0)$, which are farther away from $(-3, 0, 0.5)$, convergence to the desired exact target could not be achieved.

5 Conclusions

In this paper, the inverse geometry problem concerning for the identification of immersed obstacles in Navier-Stokes fluid flows has been investigated. First, the direct problem has been solved using the FEM to provide fluid traction on the boundary, which has then been inverted in a nonlinear least-squares sense of minimization to retrieve the desired star-shaped target obstacle of unknown centre and variable polar radius (dependent on the polar angle). The numerical results presented and discussed for Example 4.1 and 4.2 show that when the fluid traction is measured on $\Gamma_0 = \Gamma = \Gamma_{top} \cup \Gamma_{bottom} \cup \Gamma_{in}$, then the iterative FEM adaptive moment estimation algorithm described in section 3 provides accurate and robust reconstructions of a circular or cardioid obstacle parameterized by a small number of parameters (e.g., $J = 0$ or 1 in (12)). Stable reconstructions with respect to noise in the measured fluid traction data have also been achieved, although for complicated shapes parameterized by larger values of J nonlinear Tikhonov regularization of the least-squares functional (13) may need to be employed [17].

Multiple-component obstacles may also be identified, as illustrated in Example 4.3, provided that a good initial guess is provided. Finally, the case of limited data being available only at the inlet boundary Γ_{in} has been investigated in Example 4.4. For this restricted case of inverse geometric problem formulation, it was found that the pressure gradient provides more information for inversion than the fluid traction on Γ_{in}. Future work will investigate the identification of obstacles immersed in an unsteady incompressible viscous fluid [1].

Acknowledgments

This work was supported by The Scientific and Technological Research Council of Turkey (TUBITAK) [Grant Number: 1059B192000434]. No data are associated with this article. For the purpose of open access, the authors have applied a Creative Commons Attribution (CC BY) license to any Author Accepted Manuscript version arising from this submission.

References

[1] C. Alvarez, C. Conca, L. Friz, O. Kavian and J. H. Ortega (2005) Detecting an obstacle immersed obstacles via boundary measurements, *Inverse Problems*, **21**, 1531-1552.

[2] C. Alvarez, C. Conca, R. Lecaros and J. H. Ortega (2008) On the identification of a rigid body immersed in a fluid: A numerical approach, *Engineering Analysis with Boundary Elements*, **32**, 919-925.

[3] M. Badra, F. Caubet and M. Dambrine (2011) Detecting an obstacle immersed in a fluid by shape optimization methods, *Mathematical Models and Methods in Applied Science*, **21**(10), 2069-2101.

[4] M. Braack and P.B. Mucha (2011) Directional do-nothing condition for the Navier-Stokes equations, *Journal of Computational Mathematics*, **32**(5), 507-521.

[5] C. Conca, P. Cumsille, J. Ortega and L. Rosier (2008) On the detection of a moving obstacle in an ideal fluid by a boundary measurement, *Inverse Problems*, **24**, Article 045001, (18pp).

[6] C. Dapogny, P. Frey, F. Omnes and Y. Privat (2018) Geometrical shape optimization in fluid mechanics using FreeFem++, *Structural and Multidisciplinary Optimization*, **58**, 2761-2788.

[7] A. Doubova, E. Fernandez-Cara and J. H. Ortega (2007) On the identification of a single body immersed in a Navier-Stokes fluid, *European Journal of Applied Mathematics*, **18**(1), 57-80.

[8] R. Glowinski and O. Pironneau (1992) Finite element methods for Navier-Stokes equations, *Annual Reviews of Fluid Mechanics*, **24**, 167-204.

[9] F. Hecht (2012) New development in FreeFem++, *Journal of Numerical Mathematics*, **20**, (3-4), 251-266.

[10] J. G. Heywood, R. Rannacher and S. Turek (1996) Artificial boundaries and flux and pressure conditions for the incompressible Navier-Stokes equations, *International Journal for Numerical Methods in Fluids*, **22**, 325-352.

[11] A. Karageorghis and D. Lesnic (2020) Identification of obstacles immersed in a stationary Oseen fluid via boundary measurements, *Inverse Problems in Science and Engineering*, **28**(7), 950-967.

[12] A. Karageorghis, D. Lesnic and L. Marin (2021) The method of fundamental solutions for Brinkman flows. Part I. Exterior domains, *Journal of Engineering Mathematics*, **126**, Article 10, (12 pages).

[13] A. Karageorghis, D. Lesnic and L. Marin (2021) The method of fundamental solutions for Brinkman flows. Part II. Interior domains, *Journal of Engineering Mathematics*, **127**, Article 19, (12 pages).

[14] D. P. Kingma and J. Ba (2015) Adam: A method for stochastic optimization, *International Conference on Learning Representations (ICLR2015)*, 15 pages.

[15] R. Kress and S. Meyer (2005) An inverse boundary value problem for the Oseen equation, *Mathematical Methods in the Applied Science*, **23**, 103-120.

[16] W. Layton (2008) *Introduction to the Numerical Analysis of Incompressible Viscous Flows*, Society for Industrial and Applied Mathematics, Philadelphia, PA.

[17] Le Thi Hoai An, Pham Dinh Tao and Dinh Nho Hao (2002) Towards Tikhonov regularization of non-linear ill-posed problems: a dc programming approach, *Comptes rendus de l'Academie des Sciences de Paris, Series I*, **335**, 1073-1078.

[18] N. F. M. Martins and A. L. Silvestre (2008) An iterative MFS approach for the detection of immersed obstacles, *Engineering Analysis with Boundary Elements*, **32**, 517-524.

[19] B. R. Munson, A. P. Rothmayer and T. H. Okiiski (2013) *Fundamentals of Fluid Mechanics*, Wiley, New York, 7th edn.

[20] M. N. Ozisik (2000) *Inverse Heat Transfer*, Routledge, New York.

[21] W. B. Powell (2019) A unified framework for stochastic optimization, *European Journal of Operational Research*, **275**, 795-821.

[22] M. Schafer and S. Turek (1996) Benchmark computations of laminar flow around a cylinder, *Flow Simulation with High-Performance Computers II*, (ed. E.H. Hirschel), 547-566.

[23] R. Temam (1977) *Navier-Stokes Equations: Theory and Numerical Analysis*, AMS Publishing, New York.

Table 1: Target recoveries after $n_f(\rho)$ final iterations given by (17) for Example 4.1, with initial guess $(x_0^0, y_0^0, a_0^0) = (0, 0, 0.3)$.

target	prediction for no noise	prediction for 5% noise	prediction for 10% noise
$x_0 = -3$	$x_0 = -3.0116$	$x_0 = -2.9953$	$x_0 = -2.9685$
$y_0 = 0$	$y_0 = 0.0081$	$y_0 = 0.0127$	$y_0 = 0.0029$
$a_0 = 0.5$	$a_0 = 0.4961$	$a_0 = 0.5057$	$a_0 = 0.5151$

Table 2: Target recoveries after $n_f(\rho)$ final iterations given by (18) for Example 4.1, with initial guess $(x_0^0, y_0^0, a_0^0) = (5, -1, 0.3)$.

target	prediction for no noise	prediction for 5% noise	prediction for 10% noise
$x_0 = -3$	$x_0 = -3.0045$	$x_0 = -2.9943$	$x_0 = -2.9665$
$y_0 = 0$	$y_0 = 0.0098$	$y_0 = 0.0492$	$y_0 = 0.1310$
$a_0 = 0.5$	$a_0 = 0.5058$	$a_0 = 0.5062$	$a_0 = 0.5197$

Table 3: Target recoveries after $n_f(\rho)$ final iterations given by (21) for Example 4.2, with initial guess $(x_0^0, y_0^0, a_0^0, a_1^0, b_1^0) = (5, -1, 0.3, 0, 0)$.

target	prediction for no noise	prediction for 5% noise	prediction for 10% noise
$x_0 = -3$	$x_0 = -2.9909$	$x_0 = -2.9904$	$x_0 = -2.9758$
$y_0 = 0$	$y_0 = 0.0099$	$y_0 = 0.0868$	$y_0 = 0.1641$
$a_0 = 0.5$	$a_0 = 0.4991$	$a_0 = 0.5497$	$a_0 = 0.5805$
$a_1 = -0.4$	$a_1 = -0.4166$	$a_1 = -0.3665$	$a_1 = -0.3350$
$b_1 = 0.3$	$b_1 = 0.2763$	$b_1 = 0.1787$	$b_1 = 0.0989$

Table 4: Comparison of fluid traction $\boldsymbol{t}$ and ∇p components at a few points on Γ_{in}, for Example 4.4.

(x,y)	t_1	t_2	$\partial p/\partial x$	$\partial p/\partial y$
$(-7.5, 1.5)$	-5.0e-07	-1.6e-06	-4.5e-04	3.5e-04
$(-7.5, 0.5)$	-3.6e-08	9.2e-08	4.0e-04	-3.5e-04
$(-7.5, -0.5)$	-1.3e-07	-1.3e-07	4.0e-04	3.5e-04
$(-7.5, -1.5)$	-1.6e-06	1.2e-06	-4.6e-04	-3.8e-04

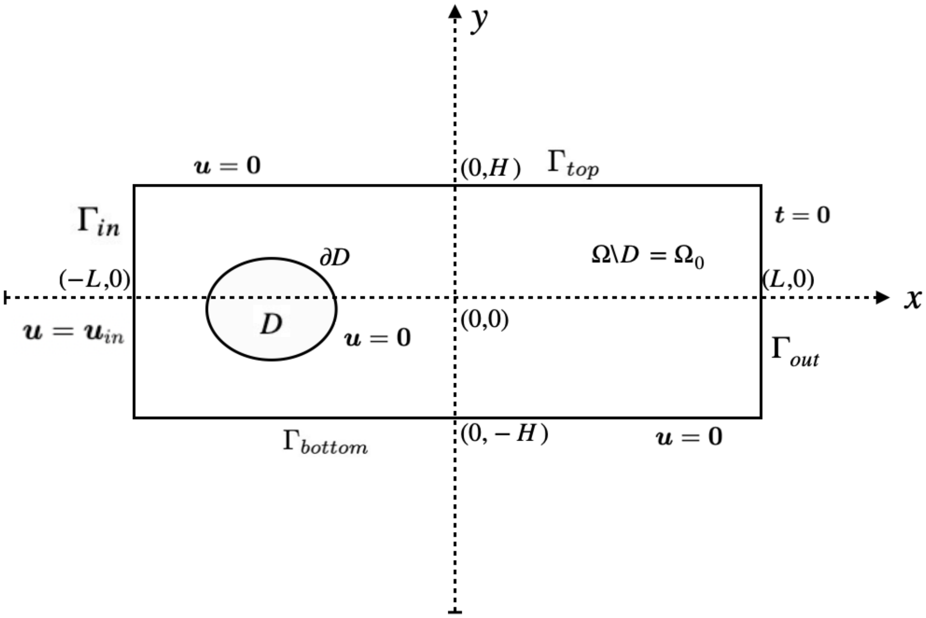

Figure 1: Schematics of the fluid domain and boundary conditions.

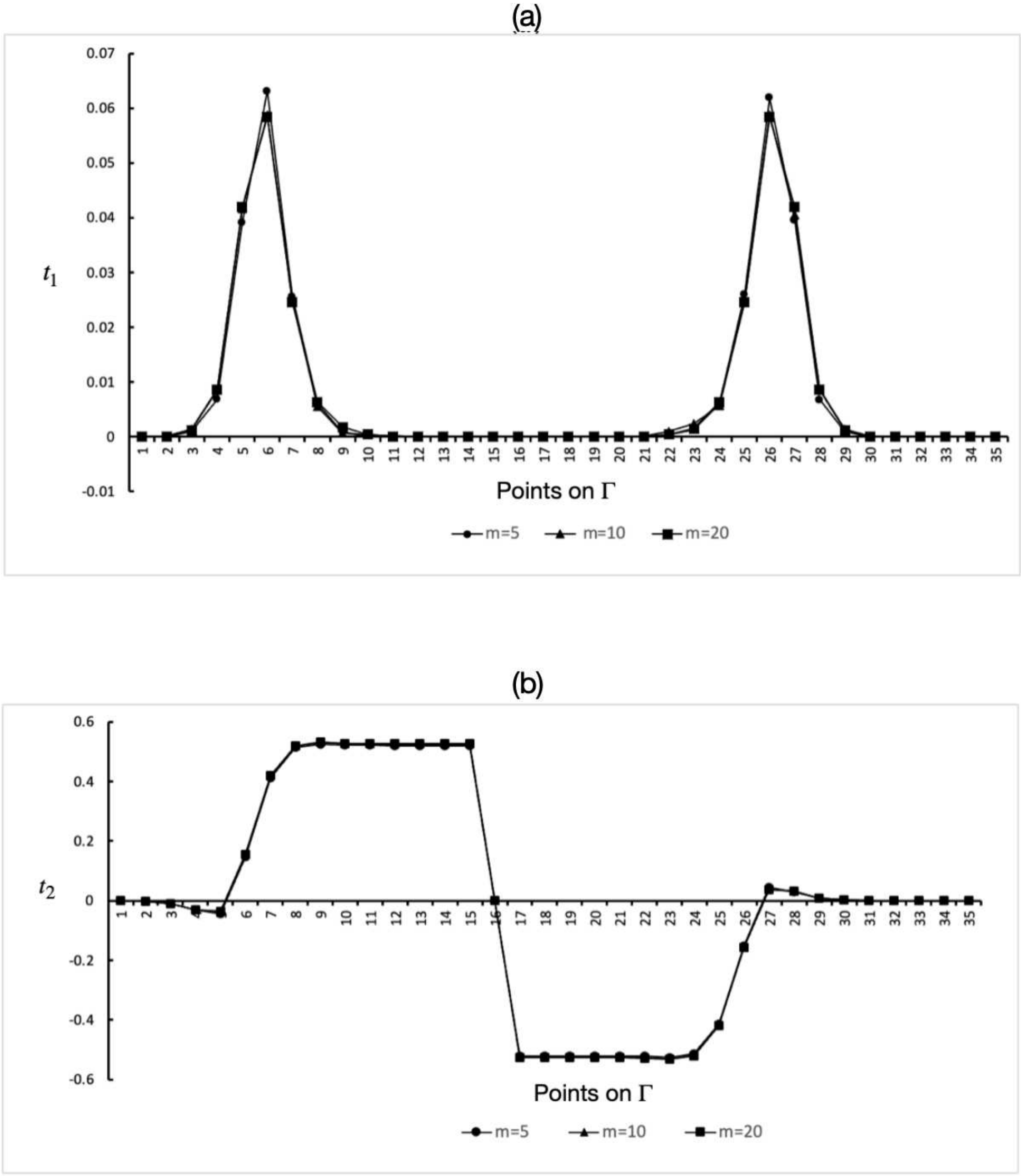

Figure 2: Illustration of mesh independency for the direct problem. (a) The comparison for the first component t_1 and (b) the second component t_2 of the fluid traction vector $\boldsymbol{t} = (t_1, t_2)$ on $\Gamma = \Gamma_{bottom} \cup \Gamma_{top} \cup \Gamma_{in}$ for $m \in \{5, 10, 20\}$. On the abscissa, the first fifteen points are on Γ_{bottom}, the next fifteen points are on Γ_{top} and the last five points are on Γ_{in}.

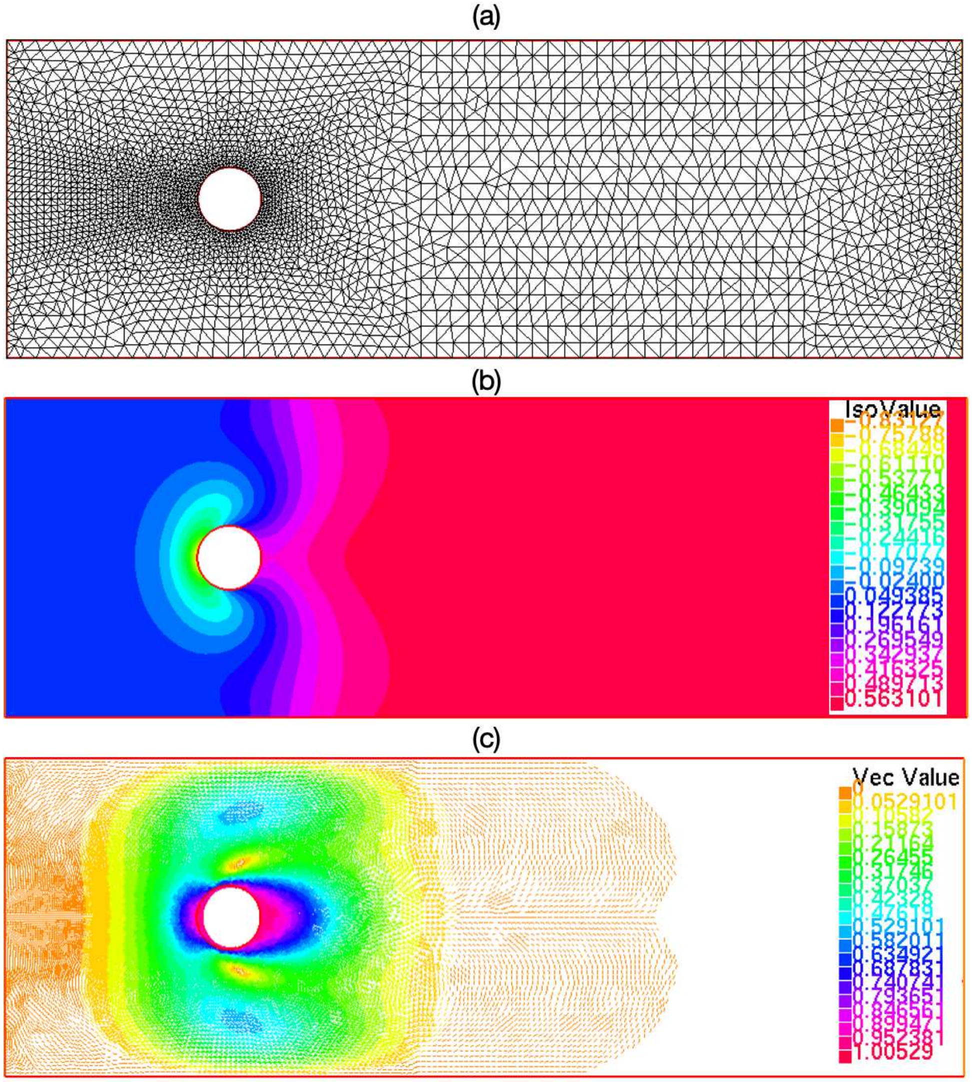

Figure 3: (a) The finite element mesh field, (b) the pressure and (c) the velocity fields for the direct problem.

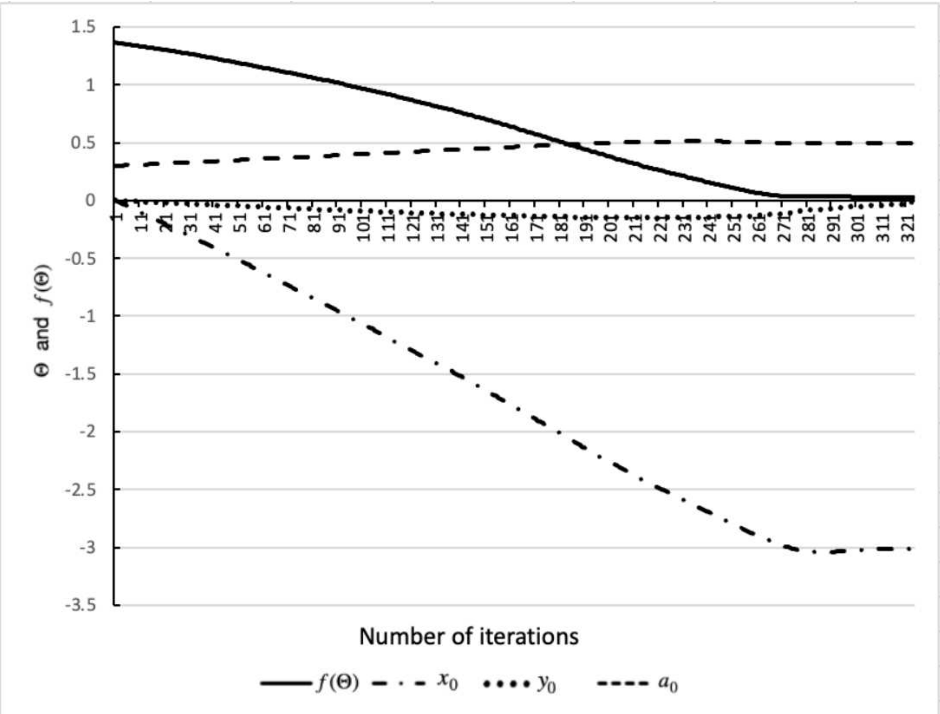

Figure 4: The objective function $f(\Theta)$ given by (13) and the obstacle's parameters x_0, y_0 and a_0 at each iteration, for Example 4.1, with initial guess $(x_0^0, y_0^0, a_0^0) = (0, 0, 0.3)$, without noise.

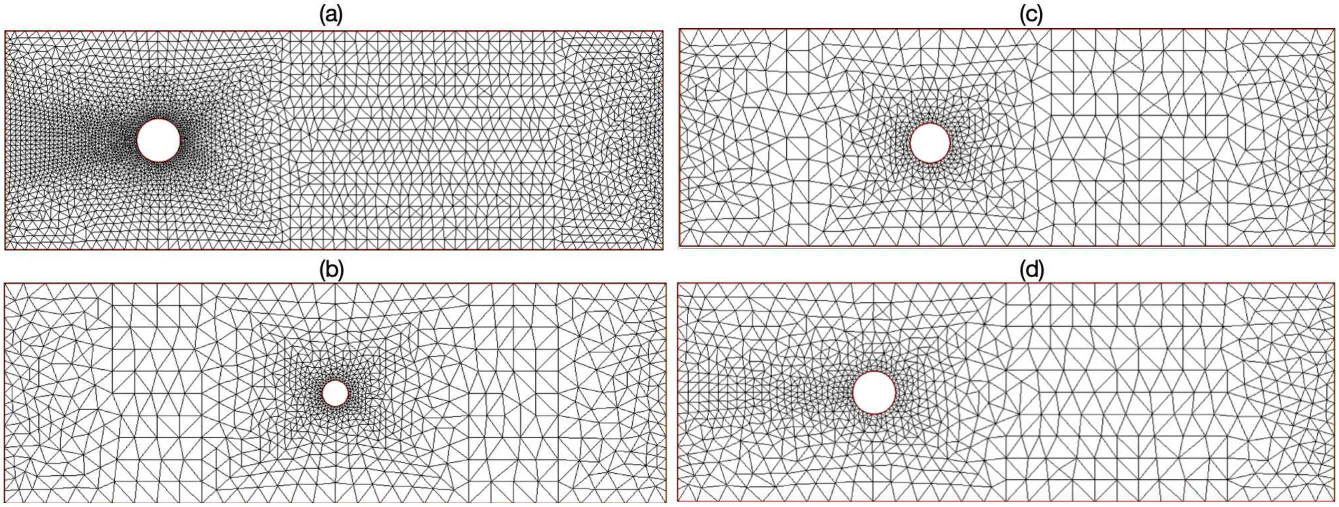

Figure 5: (a) Target obstacle, (b) initially guessed obstacle, (c) obstacle retrieved after 160 iterations and (d) obstacle retrieved after 324 final iterations, for Example 4.1, with initial guess $(x_0^0, y_0^0, a_0^0) = (0, 0, 0.3)$, without noise.

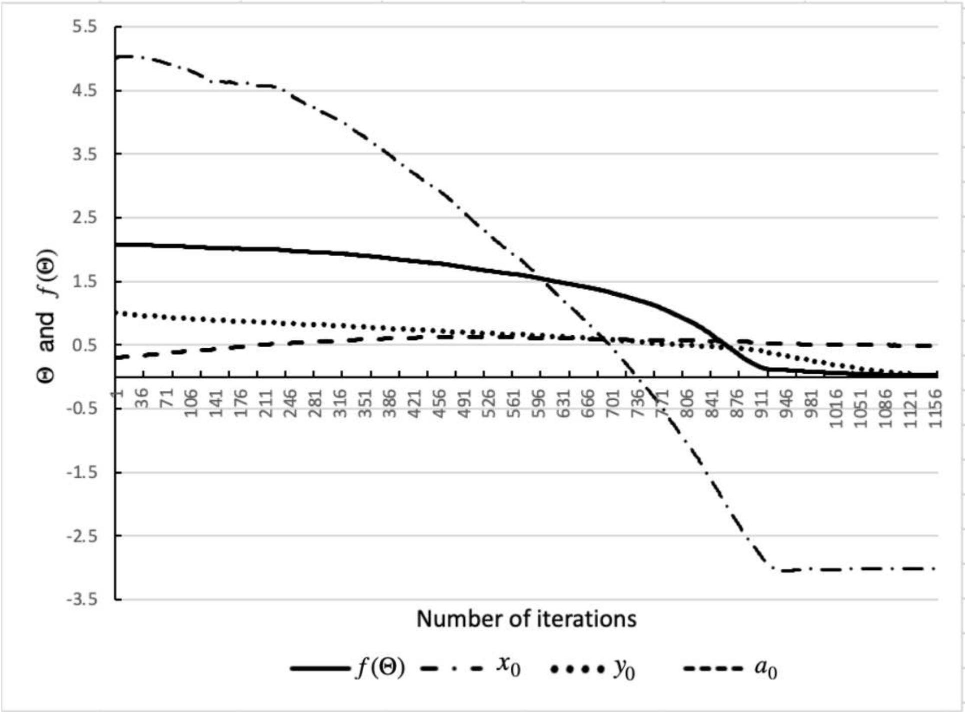

Figure 6: The objective function $f(\Theta)$ given by (13) and the obstacle's parameters x_0, y_0 and a_0 at each iteration, for Example 4.1, with initial guess $(x_0^0, y_0^0, a_0^0) = (5, 1, 0.3)$, without noise.

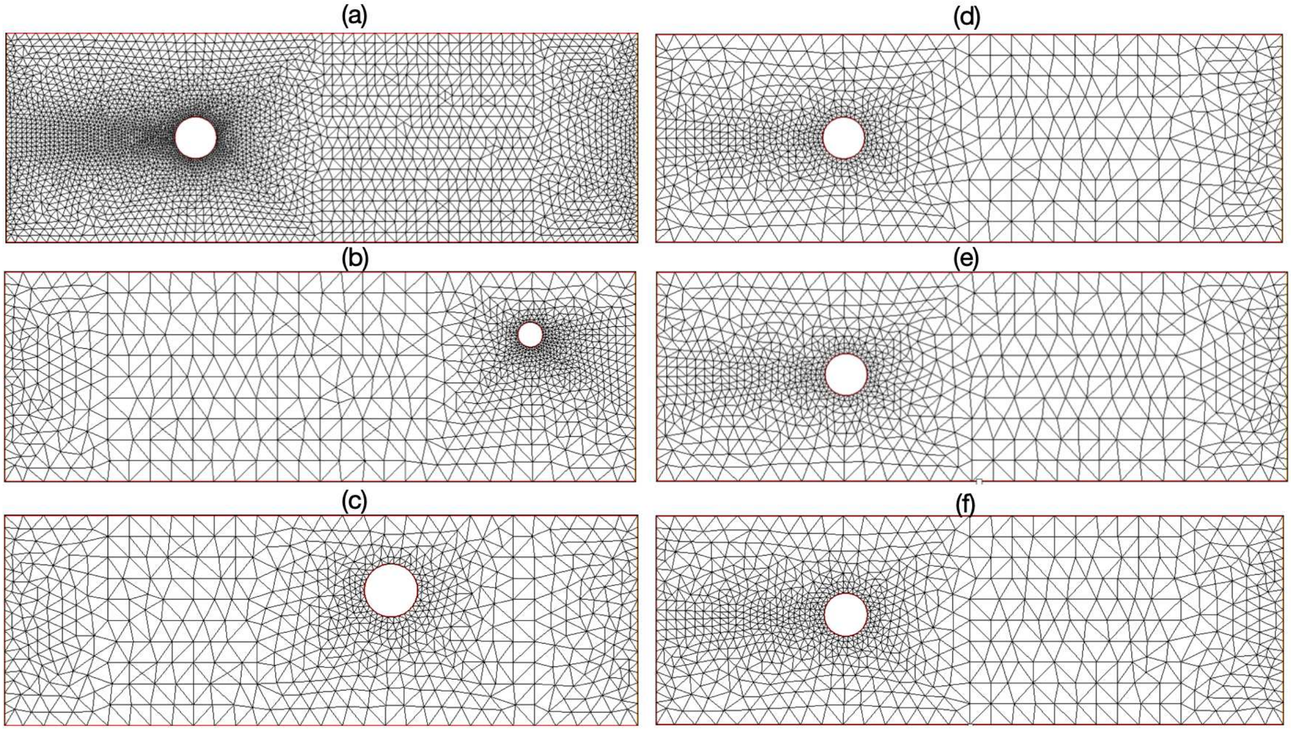

Figure 7: (a) Target obstacle, (b) initially guessed obstacle, (c) obstacle retrieved after 500 iterations for no noise, (d) obstacle retrieved after 1162 final iterations for no noise, (e) obstacle retrieved after 1349 final iterations for 5% noise, and (f) obstacle retrieved after 1112 final iterations for 10% noise, for Example 4.1, with initial guess $(x_0^0, y_0^0, a_0^0) = (5, 1, 0.3)$

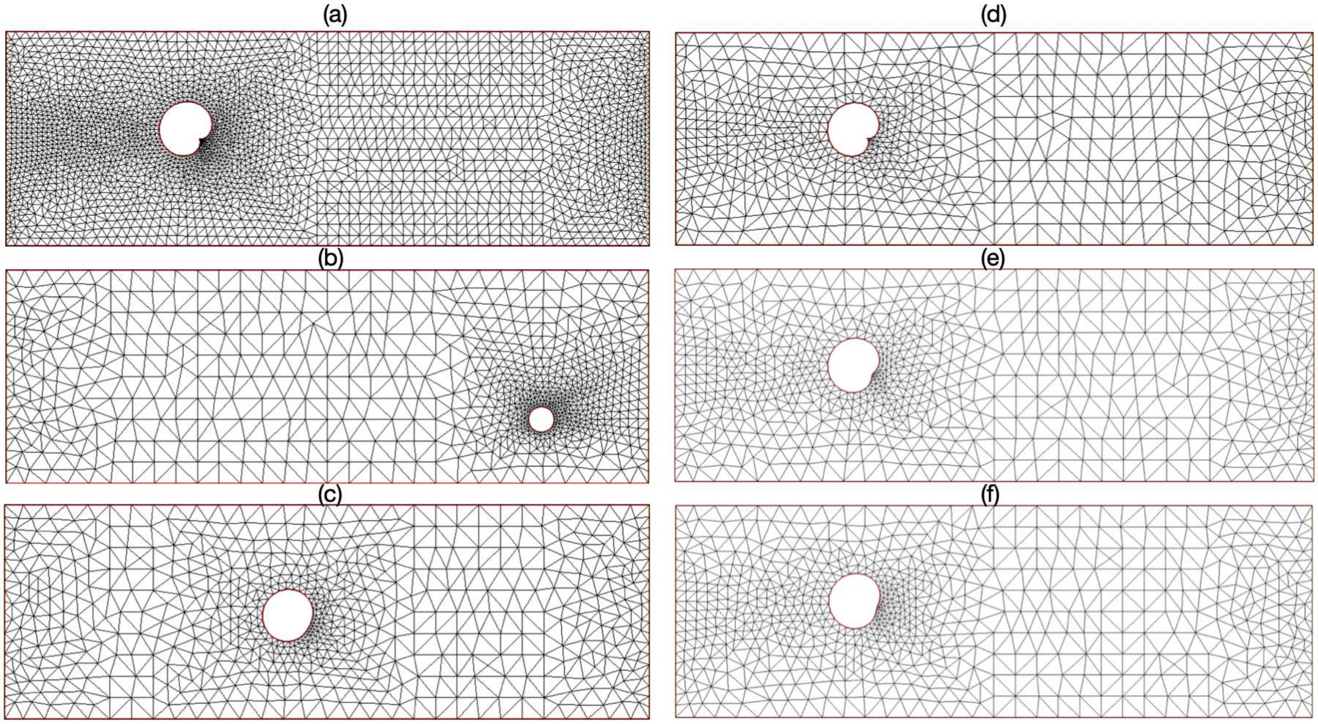

Figure 8: (a) Target obstacle, (b) initially guessed obstacle, (c) obstacle retrieved after 500 iterations for no noise, (d) obstacle retrieved after 1180 final iterations for no noise, (e) obstacle retrieved after 1052 final iterations for 5% noise and (f) obstacle retrieved after 626 final iterations for 10% noise, for Example 4.2.

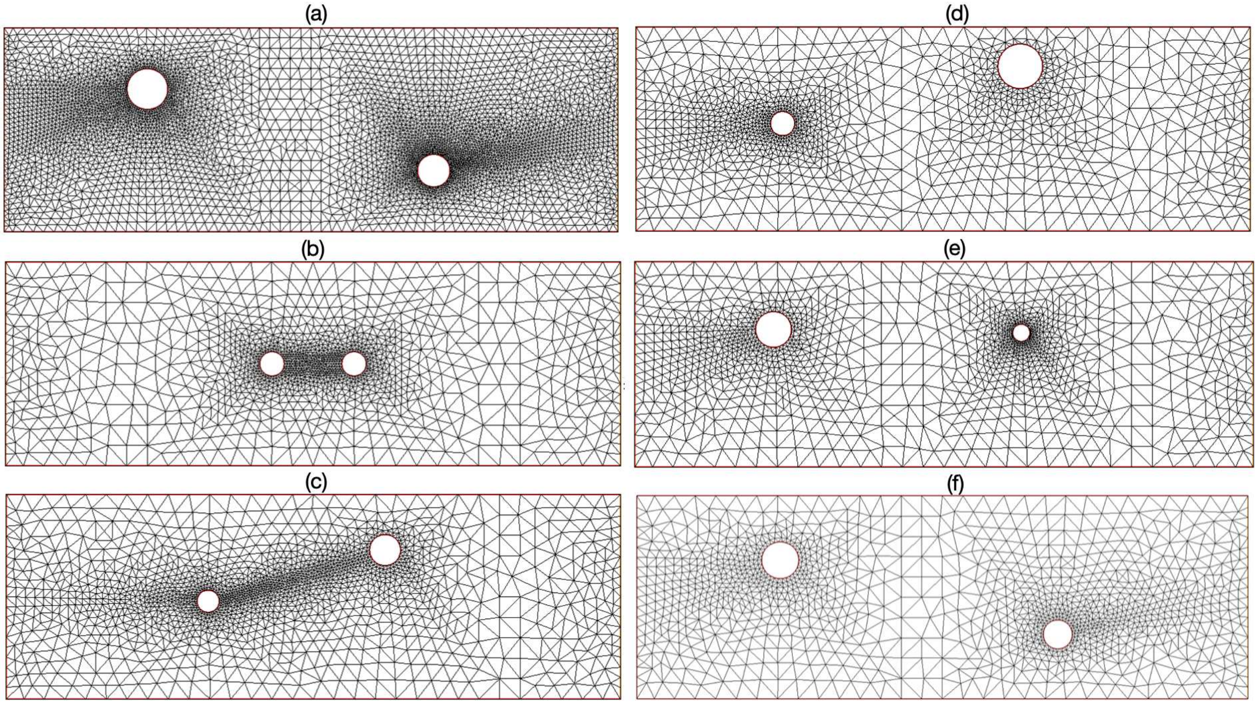

Figure 9: (a) Double-component target obstacle, (b) initially guessed obstacle, (c) obstacle retrieved after 200 iterations, (d) obstacle retrieved after 400 iterations, (e) obstacle retrieved after 600 iterations and (f) obstacle retrieved after 871 final iterations, for Example 4.3, without noise.

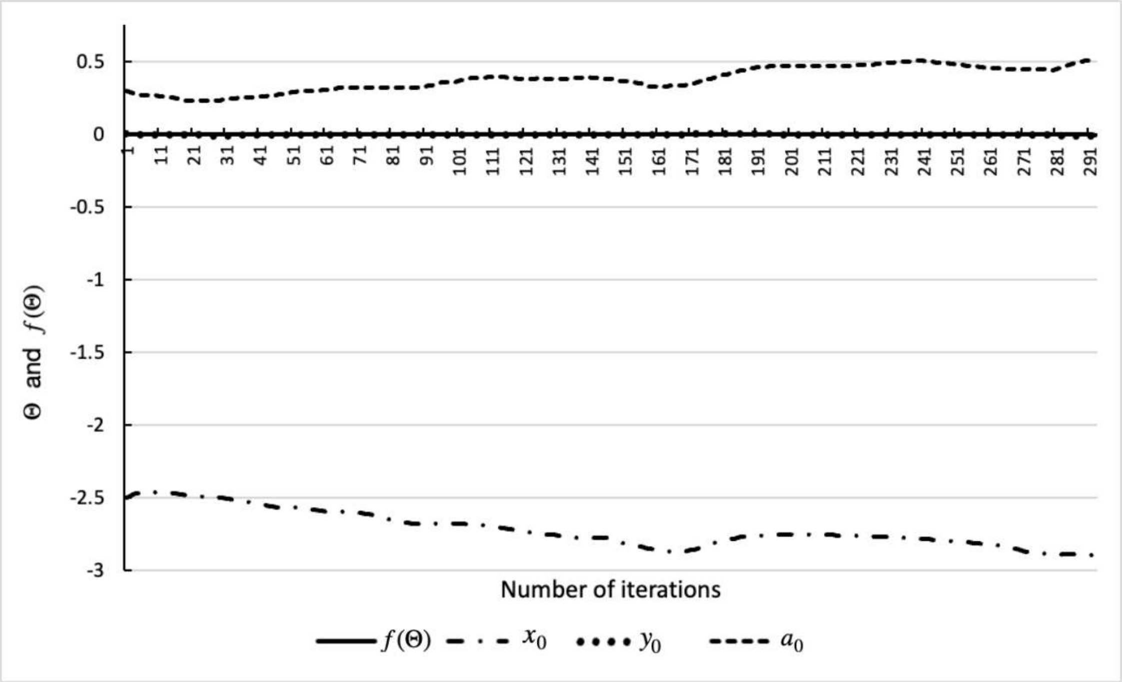

Figure 10: The objective function $f(\Theta)$ given by (13) and the obstacle's parameters x_0, y_0 and a_0 at each iteration, for Example 4.4, with initial guess $(x_0^0, y_0^0, a_0^0) = (-2.5, 0, 0.3)$, without noise.